Engineering Structures 271 (2022) 114970

Contents lists available at ScienceDirect

Engineering Structures

journal homepage: www.elsevier.com/locate/engstruct

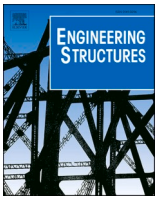

Shear strength of concrete beams using stay-in-place flexible formworks with integrated transverse textile reinforcement

Minu Lee *, Jaime Mata-Falcón, Walter Kaufmann

Institute of Structural Engineering, Swiss Federal Institute of Technology (ETH) Zurich, Switzerland

ARTICLE INFO

Keywords:
Textile reinforced concrete
Shear
Experimental study
Flexible formworks
Digital image correlation
Distributed fibre optical sensing
Crack behaviour
KnitCrete

ABSTRACT

This study investigates the fabrication and the structural performance of concrete beams using weft-knitted tubular fabrics as stay-in-place formworks with integrated textile reinforcement. The use of non-corrosive high-strength textile materials for flexible formworks offers great potential for efficient construction processes and a bespoke design of material-efficient concrete structures. To this end, an experimental campaign consisting of ten three-point bending tests on beams with rectangular cross-sections made with flexible stay-in-place formworks was conducted, where aramid rovings were integrated within the textile as transverse reinforcement to withstand the shear forces while the longitudinal reinforcement consisted of conventional deformed steel bars. The use of digital image correlation measurements and distributed fibre optical sensing allowed the refined analysis of the deformations, including the strains in the textile reinforcement and the estimation of the crack kinematics, which were used to assess various contributions from the reinforcement and the concrete to the shear strength in the governing crack. The amount of textile reinforcement proved to be a decisive parameter in increasing the shear strength, although the full tensile capacity of the rovings could not be exploited due to the lack of ductility in the material behaviour. The thorough consideration of the shear transfer mechanisms revealed a strong dependence of the concrete contribution, specifically aggregate interlock and the formation of a direct strut, on the crack patterns. The combination of the brittle aramid rovings as shear reinforcement and conventional steel reinforcing bars in the tension chord provided a large deformation capacity if the shear reinforcement was able to sustain the load until a bending failure was reached.

1. Introduction

The design of lightweight concrete structures is one of the key principles for reducing material consumption and the ecological footprint of the construction sector. Although the technological advances in construction processes, concrete mix design and structural analysis methodologies have led to a considerable improvement in material efficiency, the further optimisation of concrete structures still faces inherent challenges. The requirement for a minimum concrete cover to protect steel reinforcing bars against corrosion (usually between 20 and 60 mm, depending on building codes and exposure class) limits reducing the dimensions of concrete elements. A promising approach studied in the literature (e.g. [1–3]) and showcased in various practical applications (e.g. [4–6]) is the use of non-corrosive high-strength textile reinforcement, which typically consists of bundles of continuous filaments ('rovings') assembled in a bi-directional grid [7] and allows reducing the total concrete thickness to few centimetres. Several studies (e.g. [8–10]) have investigated the potential of such textile reinforced concrete elements in bending, proving their suitability for both ultimate and serviceability limit states by providing high strength and stiffness at a low self-weight. However, the increased complexity of formwork – especially when considering further optimisation of the beam geometry, such as a variation of the depth as suggested by [11] – presents a challenge in promoting broader use beyond niche applications. Fabric formworks provide new possibilities for material-efficient design for various structural elements, including columns, beams and slabs (e.g. [12–14]). However, the low stiffness of the fabric usually leads to large deformations of the formwork during concrete casting, which might present new facets in the design language, but is usually unwanted due to aesthetic or functional requirements.

A potential approach for improved formwork stability using flexible fabrics is the KnitCrete technology developed at ETH Zurich [15]. A

* Corresponding author.
E-mail address: mlee@ethz.ch (M. Lee).
URL: https://www.kaufmann.ibk.ethz.ch (W. Kaufmann).

https://doi.org/10.1016/j.engstruct.2022.114970
Received 17 May 2022; Received in revised form 19 August 2022; Accepted 11 September 2022
Available online 22 September 2022

weft-knitted textile is tensioned within a scaffolding frame and supported by cables or bending-active rods. It is coated with a fluid fast-setting cement paste or epoxy resin. The concrete is then cast on the stiffened fabric. The feasibility of this construction procedure on an architectural scale was highlighted in the KnitCandela pavilion [16] in Mexico City, which originated from the collaboration of the Block Research Group and Zaha Hadid Architects. However, the type and the placement of the reinforcement most suitable for such structures is still an open research question. The authors investigated the integration of high-strength fibrous materials in the knitted fabric and its activation as textile reinforcement under various loading conditions [17–19], which generally proved the feasibility of using the stay-in-place formworks as reinforcement in the final state. While these previous applications mainly focused on slab strips and shell structures, the present study investigates the potential of weft-knitted formworks with integrated textile reinforcement for linear members such as beams. The knitting procedure offers great geometric flexibility and the possibility of introducing spatial features within the fabric [20,21]. While the construction technology enables a broad spectrum of cross-section types [22], the present study focuses on reinforced concrete beams with rectangular cross-sections, where the shear reinforcement is integrated within the formwork, winding around the circumference. The simple geometry allows assessing the deformations over the full height of the specimens based on digital image correlation and fibre optical sensing, providing insight into the shear transfer mechanisms. The structural behaviour of the integrated textile reinforcement was examined in an experimental campaign consisting of ten beams in three-point bending, focussing on the mechanical activation of the textile and the estimation of the concrete contribution to the shear strength in the governing crack based on the refined analysis of the measurements. The proper understanding of the load-bearing behaviour presents a solid foundation for the further optimisation of lightweight concrete structures, leading to non-standard geometries and a substantial reduction of the material consumption.

2. Integrating high-strength rovings in tubular fabrics for stay-in-place flexible formworks

Stay-in-place formworks present many advantages where the construction needs to be fast and only limited space for additional scaffolding is available, such as in industrial buildings or bridge decks. Flat slab systems are most common, for which there is a wide variety of geometries and material combinations, including precast concrete elements with short fibres [23] or steel reinforcement [24], corrugated steel sheets [25], or beech-laminated timber [26]. While several studies in the literature have examined the potential of stay-in-place formworks for manufacturing concrete beams using textile reinforced cementitious composites (e.g. [27,28]), the direct integration of high-strength fibres within the flexible formwork is a further step in the development of lightweight concrete construction.

Previous studies on the mechanical behaviour of weft-knitted textile reinforcement in the tensile [17] and flexural [18,19] response of concrete elements concluded that the introduction of straight aramid rovings ('inlays') into a weft-knitted textile coated with epoxy resin led to the most efficient utilisation of the material strength and was best suited for the knitting procedure. Carbon and glass fibres, which are often used in conventional textile reinforcement, were less convenient to handle since they do not allow small bending radii, which may lead to damage to the fibres during manufacturing. The textiles with aramid inlays exhibited a linear-elastic behaviour and a brittle failure. The textile rovings progressively failed once the first filament reached its tensile strength due to the lack of ductility and the consequent inability to redistribute stresses within the roving cross-section. Other studies in the literature examining the behaviour of conventional textile reinforced concrete members observed this brittle type of failure in shear as well (e.g. [8–10]). *Valeri et al.* [10] concluded that adding steel reinforcement in the tension chord of the beam may significantly improve the deformation capacity in the flexural response if the textile reinforcement in the web can transfer the shear force until the bending resistance is eventually reached. Following this principle, this study focuses on the integration of high-strength aramid inlays in the weft-knitted textiles as shear reinforcement, while the bending capacity is provided by conventional steel reinforcing bars.

Tubular textiles can be shaped into any prismatic or gradually varying cross-sectional geometry by introducing shaping elements by means of cables or bending-active rods that define the vertices, as illustrated in Fig. 1a. The use of a CNC flat-bed knitting machine allows the integration of straight or curvilinear rovings (denoted as yellow lines) in the textile, winding around the whole cross-section, which ensures the enclosure of the longitudinal reinforcement and the compression zone, leading to a proper stress transfer from the transverse reinforcement to the tension chord. The variation of the connection between the inlay and the base textile along the circumference enables the design of cross-sections with inward corners (as found in T- or I-beams), with the inlay maintaining its straight course from the web to the top flange for the proper anchorage of the stirrups, as illustrated in Fig. 1a. The spacing of the inlays can be varied along the beam by changing the number of knitted rows, which allows the optimisation of the inlay layout according to the shear loading, as shown in Fig. 1b. Furthermore, the circumference of the tube may vary by increasing the number of loops within a row, which may be used for beams with variable depth, as illustrated in Fig. 1c.

However, the closed surface around the circumference requires the concrete to be filled from one end of the beam, standing upright unless the variation of inlay spacings provides zones where holes for filling the concrete could be placed. Thus, the increasing hydrostatic pressure from the wet concrete, which may lead to large deformations or even failure of the formwork, is limiting the range of feasible spans or requires the use of set-on-demand concrete solutions, as found in other approaches using ultra-thin formworks [29,30]. Furthermore, the position of the longitudinal reinforcing bars is not inherently attached to the formwork and needs to be fixed using spacers or at an external scaffold. These boundary conditions make this manufacturing procedure particularly suitable for the prefabrication of elements rather than cast-in-place applications on the construction site. The scaffolding frames may be reused in a mass-production line while providing customizability of the individual elements through the flexible formworks.

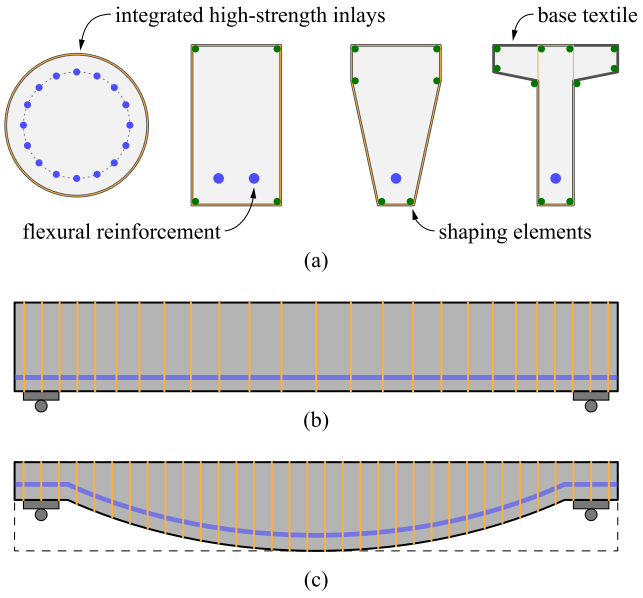

Fig. 1. Selection of feasible geometries using weft-knitted textile with integrated high-strength inlays: (a) cross-section types, (b) variation of inlay spacing, (c) beams with variable depth.

3. Experimental programme

The fabrication processes and the structural performance of stay-in-place formworks with integrated textile reinforcement were investigated in an experimental campaign consisting of ten beams. A three-point bending testing configuration was used to assess the shear capacity. The simple geometry and proper anchorage of the stirrups allowed the thorough consideration of the mechanical behaviour based on digital image correlation measurements ('DIC') and distributed fibre optical sensing ('DFOS').

3.1. Specimens, materials and manufacturing

Table 1 summarises all specimen configurations tested in this study. The nomenclature of the specimens indicates the type of textile ('R' = reference without textile, 'T' = base textile-only without high-strength inlay, and 'A' = base textile with integrated aramid inlays), the diameter of the longitudinal reinforcing bars, and the spacing of the high-strength inlays if present. The latter varied between 12 and 50 mm. Additionally, specimens without high-strength inlays, only using the textile as flexible formwork, and reference specimens without any textile, cast using conventional wooden formwork, were examined. Due to technical problems, the tests of Specimens 'A-Ø12-s30a' and 'A-Ø12-s20a' had to be interrupted, leading to an uncontrolled unloading and a subsequent reloading cycle. Therefore, these configurations were repeated to study the behaviour under monotonic loading.

3.1.1. Textiles

Following the findings from the authors' previous studies on weft-knitted textile reinforced concrete [17–19], aramid fibres with a fineness of 800 tex (1 tex = 1 g per km of yarn) were chosen for the inlay material, while the base textiles were made from non-structural acrylic yarn. The inlays had spacings of 50, 30, 20 and 12 mm depending on the specimen configuration (Table 1). The transverse textile reinforcement ratios of the rovings (ρ_{tw}) were chosen to be in the equivalent range as those suggested by building codes for conventional steel reinforcement ρ_{sw}, i.e. $\rho_{sw,min} \geqslant 0.1\%$, $\rho_{tw,min} \geqslant \rho_{sw,min} \cdot f_{su}/f_{tu} = 0.1\% \cdot 625\ \text{MPa}/2500\ \text{MPa} = 0.025\%$, where f_{tu} and f_{su} are the tensile strengths of textile and steel reinforcement, respectively. In the case of the specimens without high-strength inlays, a non-structural 'dummy' yarn at a spacing of 50 mm was used. All textiles were coated with a low-viscous two-component epoxy resin [31], developed specifically for the lamination and impregnation of textile fibres. The epoxy coating was cured for at least 24 hours at room temperature before casting. The material parameters of the coated aramid rovings were tested in separate uniaxial tension tests, as described in [17], which resulted in mean values of the tensile strength of $f_{tu} = 2583$ MPa and of the Young's modulus of $E_t = 112$ GPa.

Table 1
Specimen configurations: dimensions, inlay spacings, reinforcing bar diameters (batches in superscript), and concrete mix batches.

Specimen	b [mm]	h [mm]	d [mm]	s [mm]	ρ_{tw} [%]	$Ø_s$ [mm]	Concrete batch
R-Ø08	103.8	179.1	146.7	–	–	8	SCC-i
R-Ø12	96.0	177.8	147.9	–	–	12[a]	SCC-i
T-Ø08	105.3	178.1	150.8	–	–	8	SCC-iv
T-Ø12	105.0	185.4	151.7	–	–	12[a]	SCC-iv
A-Ø08-s50	100.2	175.9	147.0	50	0.022	8	SCC-ii
A-Ø12-s30a	101.2	175.5	147.8	30	0.035	12[a]	SCC-iii
A-Ø12-s30b	96.0	175.3	147.1	30	0.035	12[b]	SCC-iv
A-Ø12-s20a	100.9	176.5	148.3	20	0.054	12[a]	SCC-iii
A-Ø12-s20b	95.7	174.1	147.9	20	0.054	12[b]	SCC-iv
A-Ø08-s12	103.8	179.1	146.7	12	0.108	8	SCC-ii

3.1.2. Steel reinforcing bars

The longitudinal reinforcement consisted of deformed steel bars with enhanced corrosion resistance. Besides the lower feasible concrete cover, this reinforcing steel has high yield and ultimate strengths while providing relatively high ductility. The material properties were determined in tension tests on bare bars and are summarised in Table 2. Note that while the reinforcing bars with a diameter of Ø8 mm were taken from the same coil, the bars with Ø12 mm were from two different batches, resulting in slightly different material properties.

3.1.3. Bending-active glass fibre rods

The cross-sectional geometries were shaped using solid round bending-active rods, which consisted of unidirectional glass fibre rovings impregnated with a polyester resin ('GFRP') and had a diameter of Ø8 mm. The notional tensile strength and Young's modulus specified by the manufacturer were 800 MPa and 35 GPa, respectively.

3.1.4. Concrete

A self-consolidating concrete with a maximum aggregate size of 8 mm was used for all specimens. The concrete was either prepared in the laboratory using pre-mixed concrete 'Sikacrete®-08 SCC' or delivered from a local ready-mix concrete supplier, resulting in four different batches. The Young's modulus and the uniaxial compression strength were determined from three standard cylinders with a diameter of 150 mm and a height of 300 mm per batch. The tensile strength was obtained from double punch tests [32] on two cylinders with a diameter of 150 mm and a height of 150 mm per batch. The concrete was left to harden for at least 21 days before testing. The material parameters were determined on the day of the three-point bending tests; the mean values are summarised in Table 3.

3.1.5. Manufacturing of the specimens

As described in Section 2, the beams were cast upright. The longitudinal reinforcing bars and the GFRP rods for tensioning the textiles were threaded through holes in the top and bottom plate (in casting position) of the tensioning frame to fix their position, as illustrated in Fig. 2a. The bending-active rods were additionally attached to the scaffold using strings to maintain the shape over the length of the beam, as shown in Fig. 2a and Fig. 2b. The textiles were then coated with epoxy resin using brushes (see Fig. 2c). After hardening, the concrete was cast through the opening in the top plate. The nominal and actual cross-section dimensions of the tubular beams are illustrated in Fig. 3a and summarised in Table 1. The deviations in the dimensions originated from the deformations of the textile during concrete casting and the manual tensioning procedure, which, however, is expected to be a minor challenge in a more industrialised manufacturing setting, using automated tensioning devices. Local epoxy beds were cast before testing to ensure a smooth surface for the load introduction in the specimens. Additionally to providing an anchorage length of 200 mm at both ends of the beam, the longitudinal reinforcement was anchored using coupling nuts bonded to the reinforcing bar with a high-strength

Table 2
Young's modulus (E_s), yield (f_{sy}) and ultimate (f_{su}) strength, and strain at rupture (ε_{su}) of steel reinforcing bars.

Batch	E_s [GPa]	f_{sy} [MPa]	f_{su} [MPa]	ε_{su} [‰]
Ø08	182.3	741.6	861.4	47.4
Ø12[a]	180.2	724.9	853.4	60.9
Ø12[b]	167.1	651.2	791.6	61.6

Table 3
Young's modulus (E_c), cylinder compressive strength ($f_{c,cyl}$) and tensile strength (f_{ct}) of the different concrete batches.

Batch	E_c [GPa]	$f_{c,cyl}$ [MPa]	f_{ct} [MPa]
SCC-i	32.2	58.2	4.4
SCC-ii	35.2	54.9	4.3
SCC-iii	34.8	56.5	4.4
SCC-iv	37.6	69.0	5.2

injection mortar.

3.2. Test setup

All experiments were conducted in the Structures Laboratory at ETH Zurich. The beams were tested in a three-point bending configuration with asymmetric spans, as shown in Fig. 3b. The total span was 800 mm, with shear spans of 350 mm and 450 mm, resulting in shear slendernesses (a/d) of 2.3 and 3, respectively. The supports and the load application consisted of cylindrical rollers. The controlled displacement rate of the hydraulic actuator was 0.1 mm/min, whereby it was increased up to 1 mm/min during the test for specimens with large deformations (i.e. after yielding of the longitudinal reinforcement).

3.3. Instrumentation

The force measurements were taken from the load cell at the load introduction. One side face of the beam was analysed using 3D-digital image correlation ('DIC'), which allowed measuring the deformations of the beams over the surface. A pair of FLIR Grasshopper®3 cameras (4096 × 3000 px) with a focal length of 24 mm (Schneider-Kreuznach) at a stereo angle of approximately 25° were used. The field of view

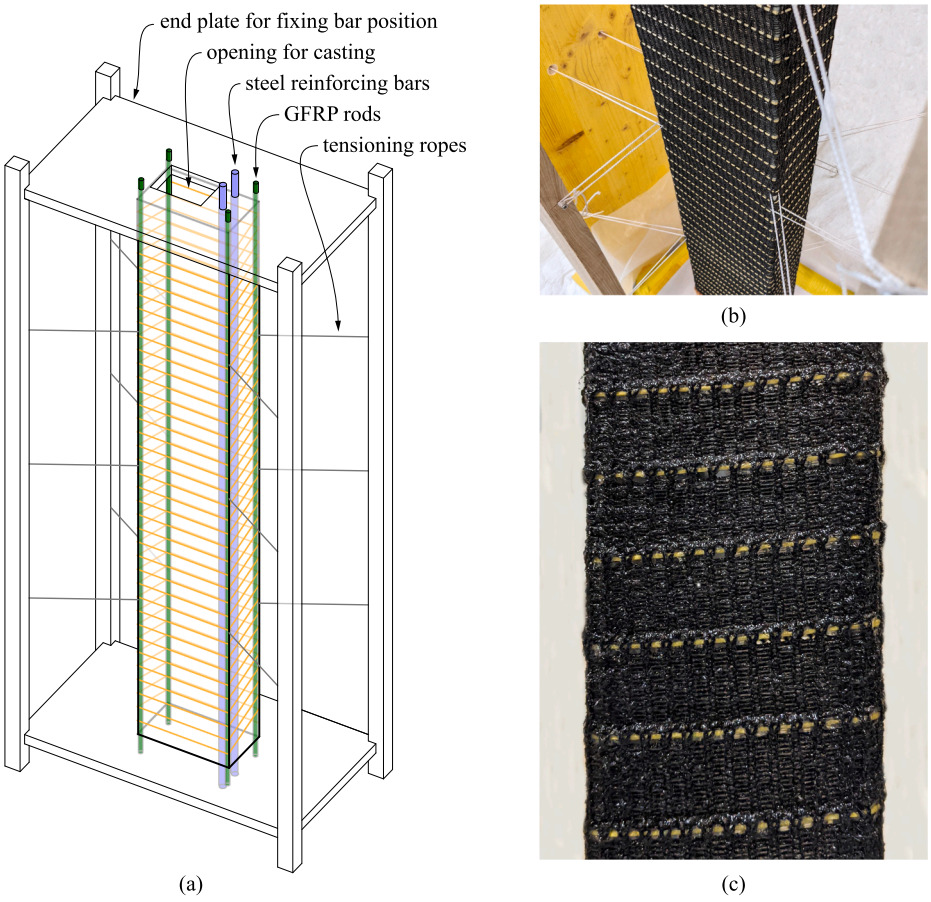

Fig. 2. Manufacturing of specimens: (a) scaffolding frame for tensioning of the textile and concrete casting, (b) tensioned textile, (c) textile with integrated aramid inlay (yellow roving) after coating.

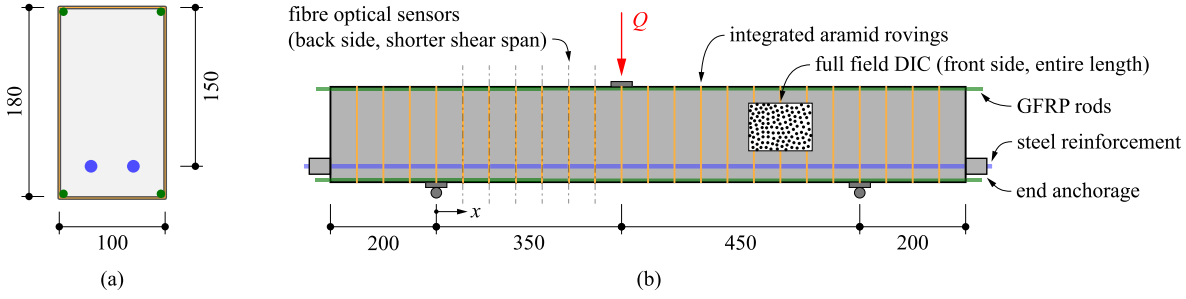

Fig. 3. Specimen configuration: (a) cross-section dimensions, (b) test setup and instrumentation (dimensions in [mm]).

covered a length of 1100 mm, leading to a resolution of 3.7 px/mm. To increase the contrast and, thus, improve the correlation, the specimens were painted white, and a random speckle pattern was applied using a stiff brush or markers, yielding speckle sizes in the range of 0.5 mm to 2 mm. The correlation was carried out with the commercial software 'VIC-3D' (Correlated Solutions Inc. [33]). The zero displacement test following [34,35] resulted in an average noise level of $\sigma(U,V) = 3 \cdot 10^{-3}$mm and $\sigma(\varepsilon_1,\varepsilon_2) = 160\,\mu\varepsilon$, using the following correlation parameters: subset size = 19 px, step size = 5 px, and strain filter size = 9. The crack behaviour was analysed with the open-source software 'Automated Crack Detection and Measurement (ACDM)' [36,37] based on the quasi-continuous displacement and strain fields from digital image correlation measurements to assess and evaluate the crack patterns and kinematics.

Additionally, fibre optical sensors were installed on the side face not instrumented with DIC to assess the deformations in the web. Bending-insensitive polyimide-coated single-mode fibres (type SM1250B3[9.8/125]P) were glued with epoxy onto the outer surface of the beam along six inlays within the shorter shear span (as illustrated in Fig. 3b) to measure the deformations of the textile reinforcement (note that in the conventional concrete reference specimens, no fibre optical sensors were installed, and that in the specimens without high-strength inlays, the sensors were uniformly distributed over the length of the short span).

4. Experimental results and discussion

This section presents the observations and results regarding the load-deformation behaviour and the failure modes of the specimens, which allows characterising the general mechanical behaviour of the tubular textiles as novel type of stay-in-place formwork and reinforcement system. The findings presented in this study generally prove the feasibility of the construction technology and highlight the particular characteristics of the reinforcement compared to conventional steel stirrups. Furthermore, the contributions from various load-bearing mechanisms are studied in more detail based on the measurements from DIC and DFOS.

4.1. Load-deformation behaviour and failure modes

Fig. 4 shows the load–deflection relationship for all specimens. The deflection was taken at the position of the load application determined from the digital image correlation measurements. All specimens with a reinforcing bar diameter of Ø8 mm (Fig. 4a) exhibited a similar behaviour in the post-cracking phase with a fairly linear load increase. Note that the elastic unloading and loading cycles – as seen in Specimen 'A-Ø08-s50′ at approximately 60 kN, for instance – were caused by relaxation when temporarily interrupting the applied displacement rate. The stiffness slightly decreased near the failure load. The specimens without high-strength inlays ('R-Ø08′ and 'T-Ø08′) and with an aramid inlay spacing of 50 mm ('A-Ø08-s50′) failed due to the formation of a diagonal shear crack, and the rupture of the textile (where present). While the failure occurred in the shorter shear span for Specimens 'T-Ø08′ and 'A-Ø08-s50′, the governing crack formed in the longer span in Specimen 'R-Ø08′, despite the 22% lower shear force. Due to the limited shear slenderness of the short span (2.3), there must have been a substantial contribution from the direct transfer of the compression force from the applied load to the support, which will be discussed in Section 5.2.2. The formation of a direct strut depends on the crack pattern and kinematics since the capacity of the concrete to transfer the compressive stresses is significantly reduced by the presence of a crack, which may explain why the governing crack occurred in the span with the smaller shear load only for a few specimens. Specimen 'A-Ø08-s12′ was the only beam failing in bending. Once reaching a local maximum of the applied force, the deformations of this beam concentrated in a single bending crack, as shown in Fig. 5a, leading to large deflections while the reinforcing bars were yielding. The specimen eventually failed due to the rupture of the steel bars. Notably, there were some distinct drops of the applied load after reaching the first local maximum.

The specimens with a reinforcing bar diameter of Ø12 mm generally displayed the same behaviour as the specimens with a bar diameter of Ø8 mm. Due to technical problems with the testing machine, Specimens 'A-Ø12-s30a' and 'A-Ø12-s20a' experienced an uncontrolled drop in the load. Fig. 4b shows only the reloading cycle, where the specimens exhibited the fully cracked stiffness from the start of the loading. In all specimens, a governing diagonal shear crack formed and the textile

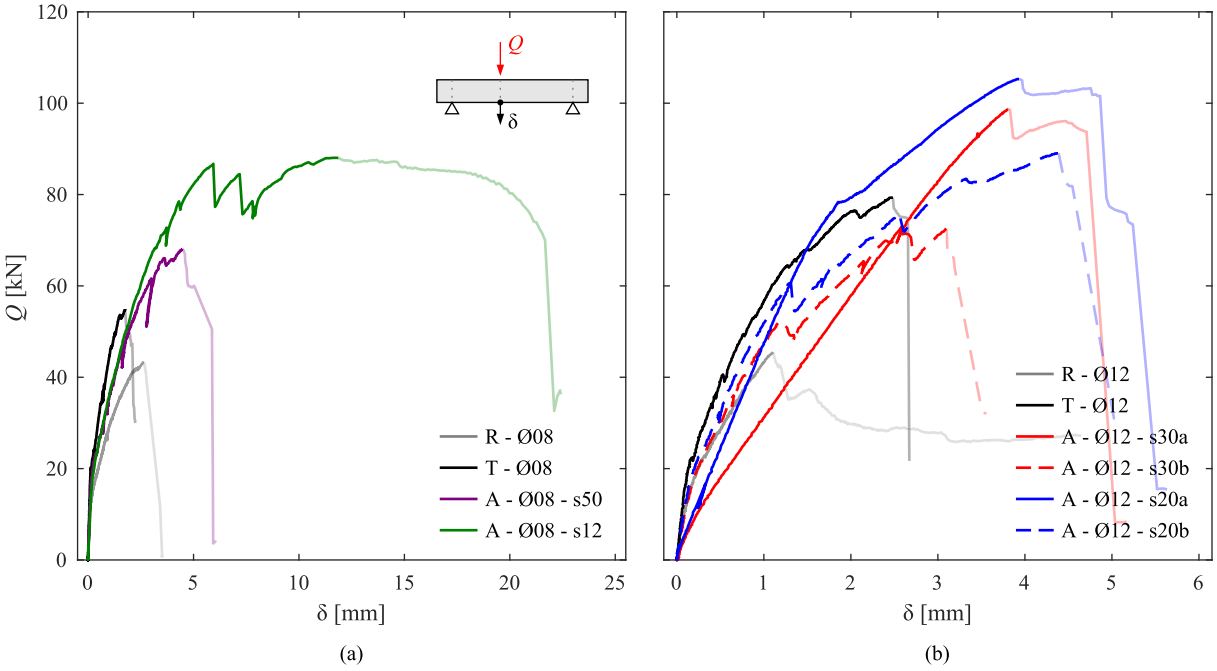

Fig. 4. Load-deflection relationship of beams with tubular textiles: specimens with longitudinal reinforcing bars with a diameter (a) Ø8 mm and (b) Ø12 mm with various transverse reinforcement ratios.

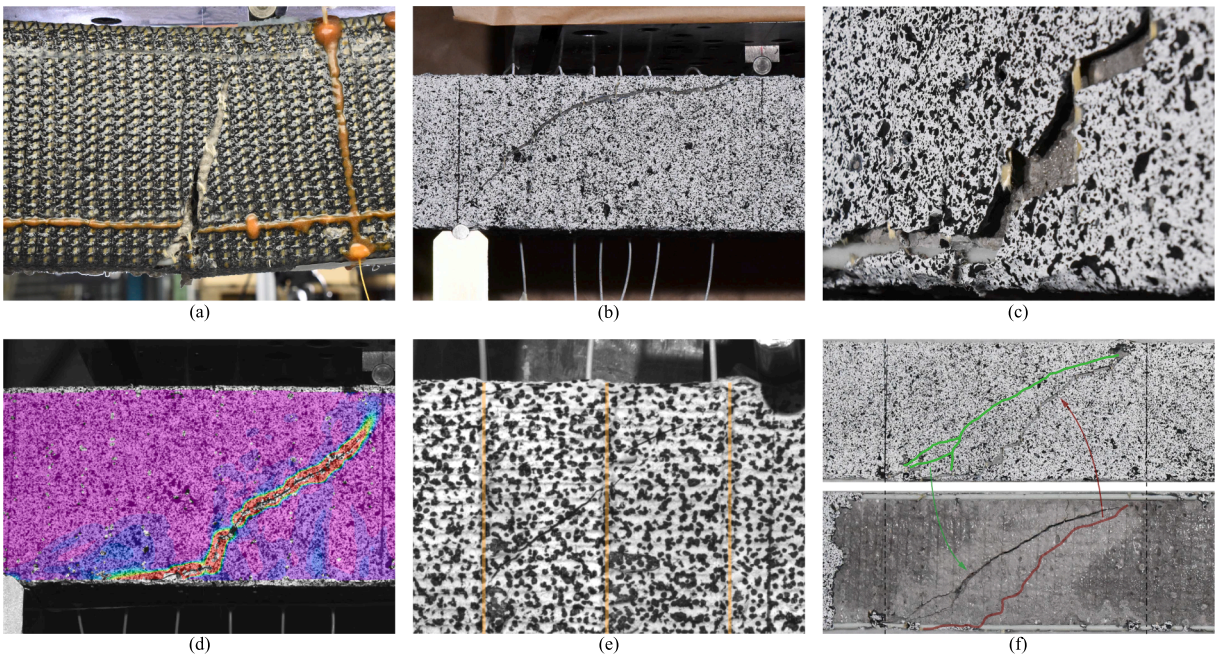

Fig. 5. Crack and failure behaviour of specimens with textiles: (a) governing bending crack in 'A-Ø08-s12′, (b) failure crack in textile ('A-Ø12-s30b'), (c) rupture of aramid inlays and base textile ('A-Ø12-s20b'), (d) crack in textile at ultimate load (before collapse) in 'T-Ø12′, (e) crack formation in base textile between two adjacent aramid inlays, denoted as yellow lines ('A-Ø08-s50′), (f) failure crack in textile (red) and governing shear crack in concrete (green) determined after stripping the textile ('A-Ø12-s30b').

ruptured where present, as shown in Fig. 5b and Fig. 5c. Specimens 'A-Ø12-s30b' and 'A-Ø12-s20b' failed in the shorter span, as expected from the higher shear force. However, the reloaded specimens with the same configurations ('A-Ø12-s30a' and 'A-Ø12-s20a') exhibited the governing crack in the longer span, considerably exceeding the failure load attained in their monotonically loaded counterparts, as shown in Fig. 4b. The higher shear force in the shorter span was presumably resisted by a significant contribution from the concrete to the shear transfer across the governing crack, which will be discussed in Section 5.2.

As expected, the reference specimens without textile displayed the lowest failure load, and the shear force at ultimate load increased with the number of transverse aramid rovings, as shown in Fig. 6 and summarised in Table 4. However, the specimen with only the textile and without high-strength inlays ('T-Ø12′) exhibited a surprisingly high failure load, even exceeding the ones of the specimens with transverse reinforcement at spacings of 50 and 30 mm. While the slightly larger cross-sectional dimensions, as presented in Table 1, and the higher strength of the concrete compared to the reference specimen without textile (see Table 3) are potential reasons for this unexpected result, a direct strut or dowel action might have had a substantial contribution to the shear strength, which will be discussed in more detail in Sections 5.2 and 5.3, especially considering that a significant diagonal crack had already formed in the textile, as shown in Fig. 5d.

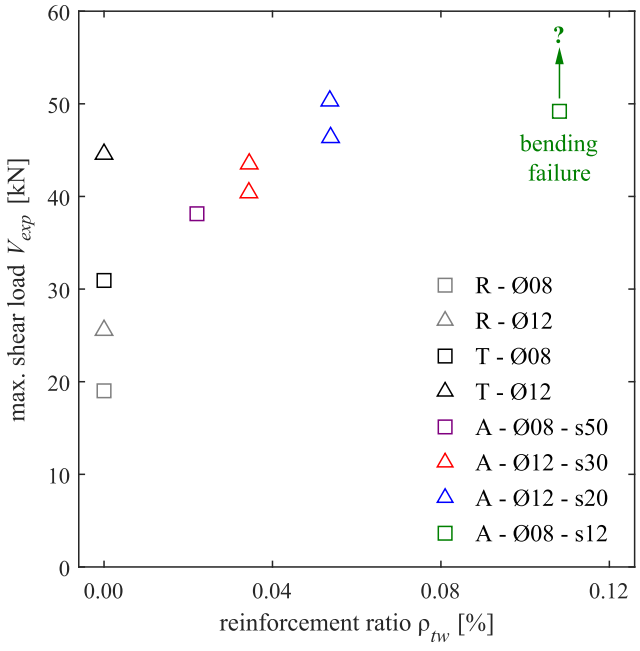

Fig. 6. Maximum shear load V_{exp} vs transverse reinforcement ratio ρ_{tw}.

4.2. Behaviour of the tension chord and contribution from GFRP rods

The deformations in the tension chord were determined using the digital image correlation measurements based on the methodology presented in [18]. The linear moment distribution in the beam leads to a parabolic change in the elongation of the reinforcement when assuming a fully cracked beam, which is nearly linear in the proximity of the

Table 4
Contributions to the shear transfer across the governing crack (excluding other sources such as direct strut and residual tensile stresses in the fracture process zone) and comparison with experimental values.

Specimen	V_{exp} [kN]	$V_{tw,nom}$ [kN]	V_{tw} [kN]	V_{ag} [kN]	V_{dow} [kN]	$\sum V_i$ [kN]	$\sum V_i/V_{exp}$ [-]
R-Ø08	19.0	–	–	20.3	1.9	23.0	1.21
R-Ø12	25.6	–	–	12.4	6.3	19.3	0.75
T-Ø08	30.9	–	–	0.0	8.5	8.5	0.27
T-Ø12	44.6	–	–	6.9	20.0	26.9	0.60
A-Ø08-s50	38.1	14.4	7.2	2.5	8.1	17.8	0.47
A-Ø12-s30a	43.5	28.7	11.0	0.3	1.3	12.6	0.29
A-Ø12-s30b	40.4	23.0	10.1	0.5	2.1	12.7	0.31
A-Ø12-s20a	46.4	37.3	14.3	0.0	2.8	17.0	0.37
A-Ø12-s20b	50.3	30.1	19.6	0.6	9.7	29.8	0.59

maximum bending moment. Hence, the mean steel strains (ε_{sm}) were estimated by applying linear regression on the horizontal displacements obtained from DIC at the depth of the steel reinforcing bars in the range where the applied bending moment exceeded 80% of the maximum loading. The depth of the compression zone (x_c) resulted from the DIC measurements of the crack openings within the region where the bending moment extended above 80% of the maximum and the length of the cracks exceeded half the specimen height, assuming linearly opening cracks and applying linear regression to obtain the location of the crack tip as described in [18]. The strains in the GFRP rods (ε_{gf}) were then determined assuming a linear strain variation over the depth, as illustrated in Fig. 7a. It was assumed that the GFRP rods could be activated fully in tension at the cracked cross-section due to their presumably rigid glued connection to the textile. However, the bond conditions of the GFRP rods are difficult to assess since the contact surface with the concrete is limited, and the surface texture of the rods is smooth, leading to a low stress transfer between the rods and the concrete. Therefore, it was assumed that the GFRP rods exhibited zero tension stiffening. The stresses in the steel reinforcement were determined by applying moment equilibrium on the cracked cross-section, as illustrated in Fig. 7a, assuming linear behaviour of the concrete and the GFRP rods, which yielded.

$$\sigma_s = \frac{\frac{Q \cdot a \cdot (l-a)}{l} - A_{gf} \cdot \varepsilon_{gf} \cdot E_{gf} \cdot \left(d_{gf} - \frac{x_c}{3}\right)}{A_s \cdot \left(d_s - \frac{x_c}{3}\right)} \quad (1)$$

where Q = applied load, a = shorter shear span, l = total span, A_{gf} = cross-sectional area of the GFRP rods, ε_{gf} = strains in the GFRP rods, E_{gf} = Young's modulus of the GFRP rods, d_{gf} = static depth of the GFRP rods, x_c = depth of the compression zone, A_s = cross-sectional area of the steel reinforcing bars, d_s = static depth of the steel reinforcing bars.

Note that the derivation of the steel stresses is only valid as long as the deformations do not concentrate in a single crack. The resulting stress–strain relationships of the steel reinforcing bars are shown in Fig. 7b and c, where the tensioning stiffening effect ($\Delta\varepsilon$ in tension, and $\Delta\chi = \Delta\varepsilon/(d-x)$ in bending as illustrated in the moment–curvature diagram in Fig. 7a) is visible as a reduction of the mean strains in the tension chord compared to the bare steel at the same stress level. The contribution of the GFRP rods (denoted as green line in Fig. 7a) to the total bending moment (denoted as black line) obtained using Eq. (1) at 90% of the ultimate load was around 20% for the specimens with a longitudinal reinforcing bar diameter of Ø8 mm and around 10% with Ø12 mm. The analysis of the crack openings of the bending cracks (denoted as grey lines) for Specimen 'A-Ø08-s12′ in Fig. 8a shows that the deformations at peak load were mainly concentrated in a single crack (denoted as red line). Despite the large crack opening, the GFRP rods did not rupture. The shape of the governing bending crack at various load levels (Fig. 8b) shows the contribution from the GFRP rods in tension since bending cracks would typically exhibit a linear opening (extrapolation shown as dashed line). The distinct drops of the load in Specimen 'A-Ø08-s12′ and its capability to further increase the load suggest that some damage to the GFRP rods or their connection to the textile might have occurred prior to the rupture of the steel reinforcement.

4.3. Activation of the textile reinforcement

Most applications of digital image correlation for testing structural concrete usually aim to detect the crack pattern and measure the crack opening and slip [35]. Here, in contrast to conventional reinforced concrete structures, the weft-knitted textile reinforcement covers the outer surface of the beam, allowing the direct measurement of the reinforcement strains using DIC, but complicating the determination of crack kinematics from the measurements. Fig. 9 shows the principal strains (ε_1) at 50% and 100% of the ultimate load for selected beams. The crack patterns were clearly visible for the reference specimen without textile ('R-Ø12′) at both load levels: the concentrated deformations due to the presence of the opening cracks are represented as high strain areas; note, however, that the concept of strain is meaningless across cracks. In the measurements of the beams with textiles, the bending cracks were still distinguishable at the lower load level. However, the strains spread over larger areas at the ultimate load. While the cracks could be determined using ACDM when they initially formed, denoted as grey lines in Fig. 9b, no individual cracks were detectable at ultimate load in the specimens with a high transverse reinforcement ratio (e.g. 'A-Ø12-s20b'). Since there were no spatial features to enhance the mechanical interlock between textile and concrete, as presented in previous studies [19], bond relied on adhesion and friction alone, leading to the debonding of the textile from the concrete with increasing deformations. The proper anchorage around the cross-section ensured the mechanical activation of the aramid inlays, and the debonding led to a more uniform distribution of strains over the height of the beam instead of concentrating them in the vicinity of the crack as in stirrups fully embedded in the concrete.

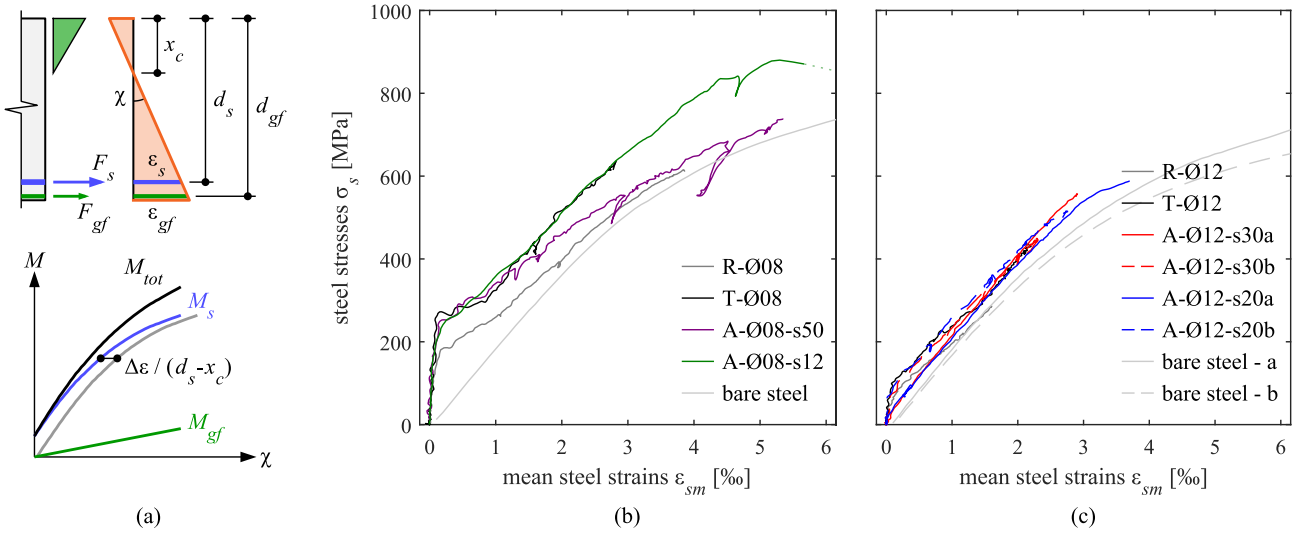

Fig. 7. Behaviour of the tension chord: (a) stress and strain state in cracked cross-section and resulting moment–curvature relationship (considering different contributions from steel reinforcement and GFRP rods), and stress–strain relationships of steel reinforcement in specimens with bar diameter of (b) Ø8 mm and (c) Ø12 mm compared to bare steel (denoted as grey lines).

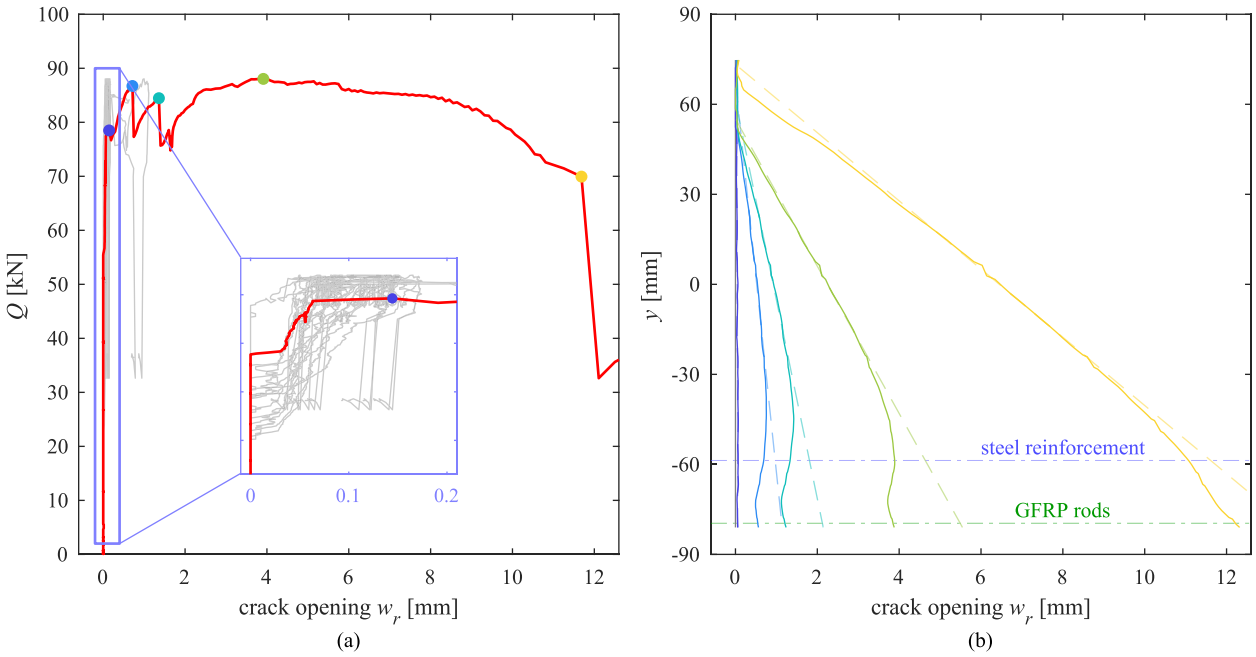

Fig. 8. Analysis of bending cracks of Specimen' A-Ø08-s12′: (a) applied load Q vs crack openings w_r for all cracks (grey: all bending cracks; red: governing bending crack), and (b) crack opening over the specimen height of the governing bending crack at various load levels.

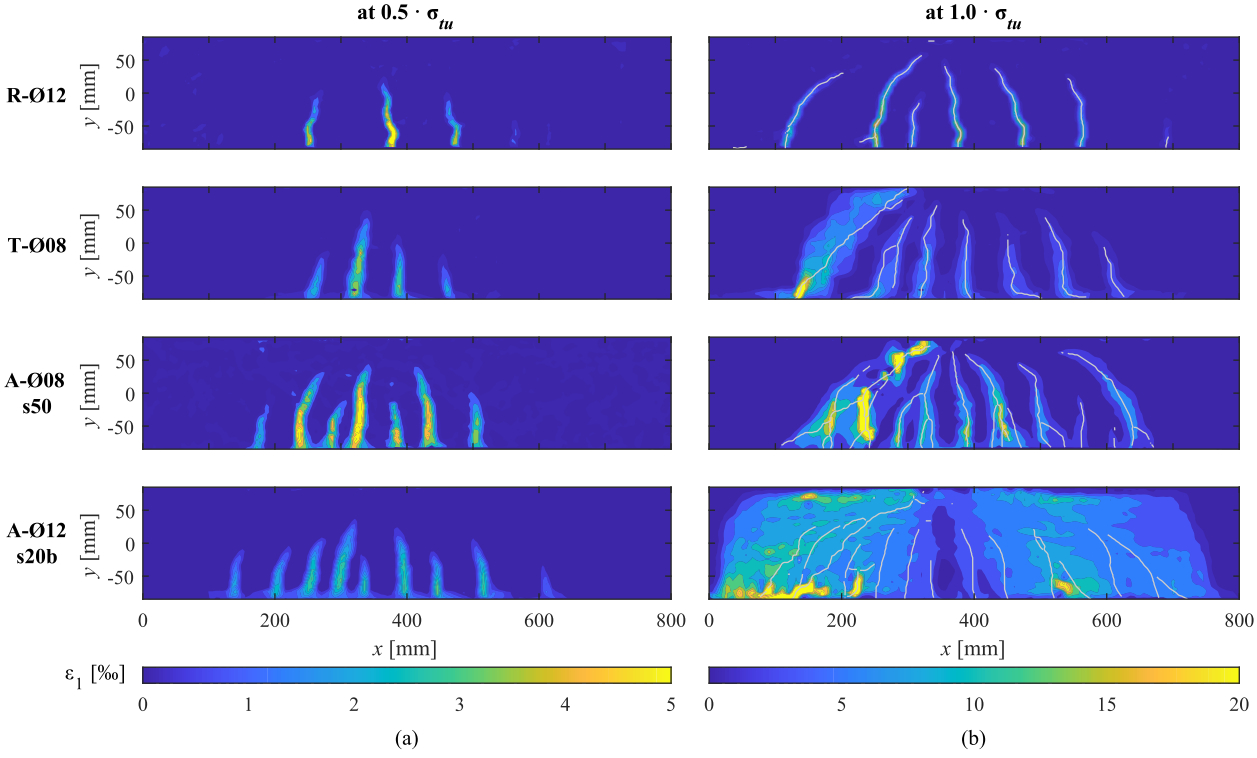

Fig. 9. Principal tensile strains (ε_1) on the surface for selected beams at (a) 50% and (b) 100% of the ultimate load and cracks determined at initial formation (denoted as grey lines).

Due to the brittle material behaviour of the aramid inlays, the full tensile capacity of the shear reinforcement could not be activated since a progressive failure occurred once the first roving reached its tensile strength. As illustrated in Fig. 10, which shows the strains in vertical direction (ε_{yy}), the textile reached the failure strain (i.e. $\varepsilon_{tu} = f_{tu}/E_t = 2.31\%$) only in locally limited areas at the ultimate load. This observation was confirmed by the fibre optical measurements on the opposite side, shown in Fig. 10. The distribution of strains was more pronounced in the specimens with higher transverse reinforcement ratios (i.e. spacings of 30, 20 and 12 mm) than in the specimens with no or fewer inlays, where the activation of the textile did not propagate over the full height of the beam. Specimen 'T-Ø12′, which had displayed a surprisingly high failure load, even exhibited the formation of a distinct diagonal shear crack in the textile before failure, as shown in Fig. 10, which

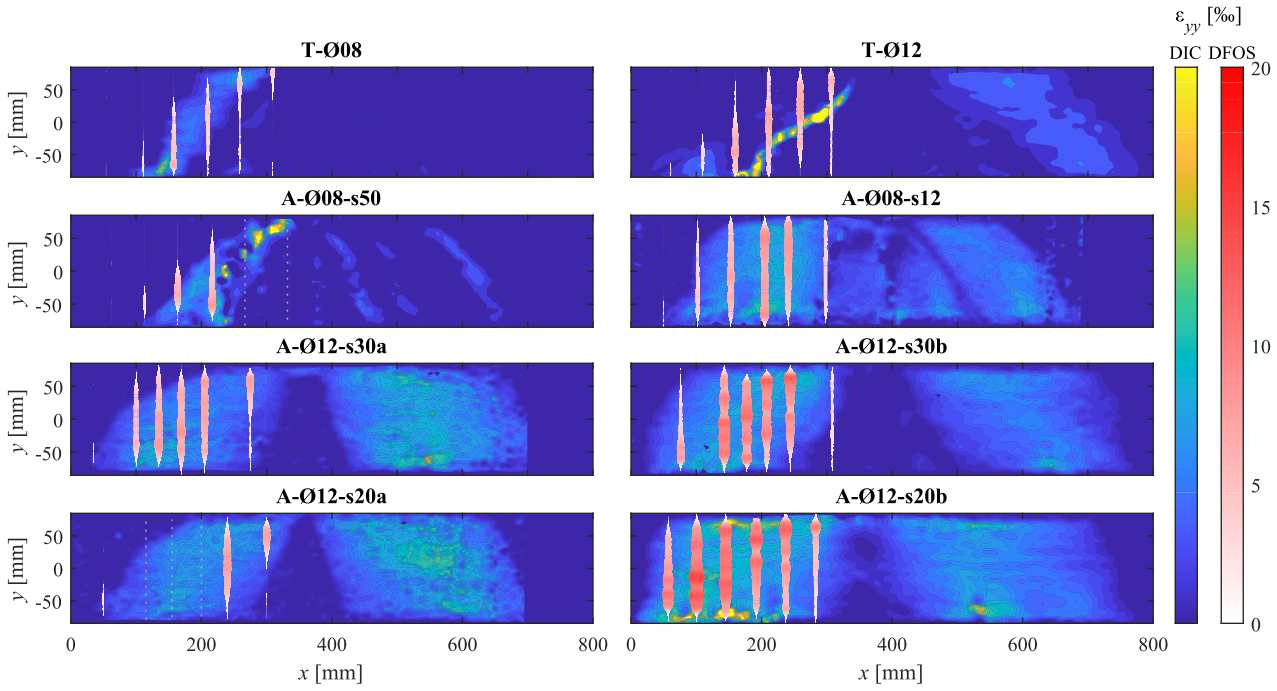

Fig. 10. Strain measurements using digital image correlation and distributed fibre optical sensing (dotted grey lines denoting where the signal was lost) at ultimate load for specimens with tubular textiles (with and without high-strength inlays).

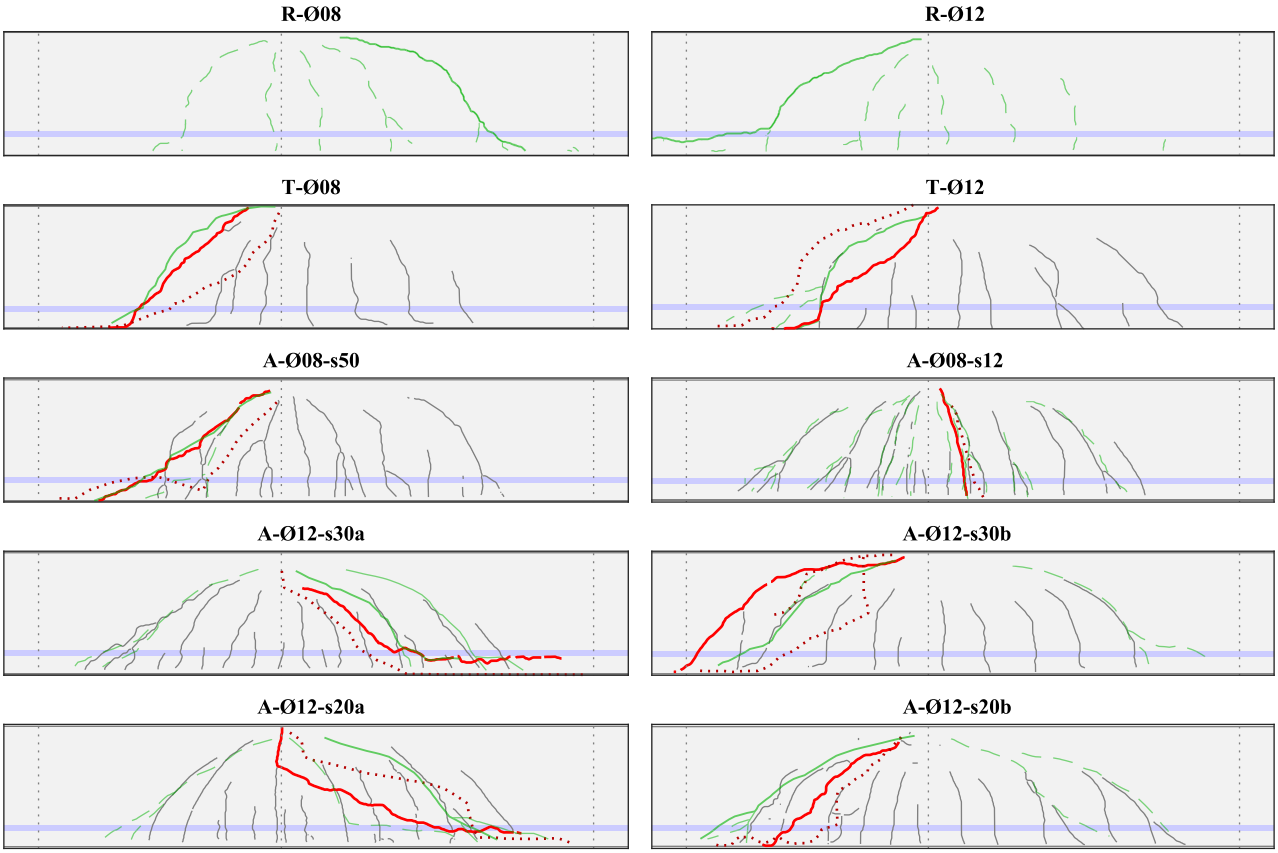

Fig. 11. Crack patterns of all specimens with the governing crack in the concrete as solid green line, secondary concrete cracks as dashed lines, the failure cracks in the textiles as red lines (solid on front side, dotted on back side of the specimen), and the cracks in the textile determined at the last load stage before debonding as grey lines.

supports the suggestion described in Section 4.1 of a substantial contribution from the concrete in the shear transfer across cracks. The strains in the textile rovings in the shorter spans for the specimens that needed to be reloaded ('A-Ø12-s30a' and 'A-Ø12-s20a') were generally lower at ultimate load than in their counterparts ('A-Ø12-s30b' and 'A-Ø12-s20b'), suggesting a larger contribution from the concrete to the shear capacity in the shorter span and explaining the different failure locations in the reloaded and monotonically loaded specimens, respectively.

4.4. Crack kinematics

While the initial crack pattern could be determined at lower load levels with DIC and ACDM, as described in Section 4.3, the further propagation of the governing cracks could not be detected due to the smearing of deformations over the area of interest by the tubular textiles. Therefore, the measurements of the actual opening and slip of the crack in the concrete, which are essential for estimating the shear transfer across cracks by specific mechanisms such as aggregate interlock, exhibit high uncertainty depending on the degree of debonding of the textile. While the governing crack (in the concrete) opened in the textile between adjacent high-strength inlays in Specimen 'A-Ø08-s50′ as well, see Fig. 5e, the specimens with closer inlay spacing (i.e. 30 and 20 mm) usually did not exhibit visible shear cracks in the textile before failure. After testing, the textile was stripped from the specimens, and the crack pattern and the location of the governing cracks were determined by visual inspection of the concrete surface, as shown in Fig. 5f. Only cracks with a substantial opening at failure could be detected since most cracks closed again when unloading the specimen and were not recognisable by eye after the test. Fig. 11 shows the initial crack patterns on the textile surface obtained from DIC (grey lines), the failure crack in the textile (red lines, with the solid and dotted lines indicating cracks in the textile on the front and back side of the specimen, respectively), and the manually determined cracks in the concrete after testing (green lines, governing crack as solid and secondary cracks as dashed lines). In the case of the reference specimens ('R-Ø08′ and 'R-Ø12′, top row in Fig. 11), the crack patterns were directly obtained from the concrete surface using the DIC-based ACDM approach. In most specimens, the cracks in the concrete generally coincided well with the initial crack pattern obtained from the DIC measurements of the textile, whereby the shear cracks propagated further up the beam. The failure cracks in the textile usually did not follow the shear crack in the concrete and exhibited different shapes on the front and back side of the specimen.

Despite the lack of direct measurements, the crack kinematics can be estimated by the total vertical deformation of the beam along its axis, which can be determined from the relative displacements of the top and bottom edge of the specimen, as illustrated in Fig. 12a, and corresponds to the total vertical component of the crack opening of all cracks crossing the section. Fig. 12 shows the maximum vertical crack displacement against the shear load in the governing span. The crack opening at failure generally increased with the transverse reinforcement ratio. The initial formation of the shear crack is visible as an increase in the vertical crack component. Specimen 'A-Ø12-s30a' had to be reloaded, and the shear crack had already formed in the first loading cycle, which explains the opening of the crack at already low load levels. The specimens that exhibited an early debonding of the textile once the shear crack started forming (e.g. 'A-Ø12-s30b' or 'A-Ø12-20a/b') exhibited only a slight increase or even a decrease of force with the initial opening of the crack, which may have been caused by the need for deformations to either activate the textile reinforcement or the stresses in the crack through aggregate interlock. The specimens with a lesser degree of debonding – namely 'A-Ø08-s50′ and 'T-Ø12′ – showed a steeper increase of shear load with increasing crack opening, which might suggest that – despite the smaller transverse reinforcement ratio – other shear transfer mechanisms such as a direct strut might have contributed to the load-bearing behaviour, as will be discussed in Section 5.2.

Measuring the deformations of the concrete surface in the reference specimens using DIC and analysing them with ACDM directly yields the crack kinematics, as illustrated in Fig. 13a. While this direct method cannot be used in the specimens with tubular textiles, as the latter debond from the concrete, the crack opening and slip in these specimens can be estimated from the vertical crack component. Assuming that the opening of the crack is caused by a rotation around the crack tip, as described in [38], the opening (δ_n) and slip (δ_t) can be determined as the components of the crack opening vector, which is defined by its vertical component ($\Delta\delta$) and the position of the rotation centre defining its

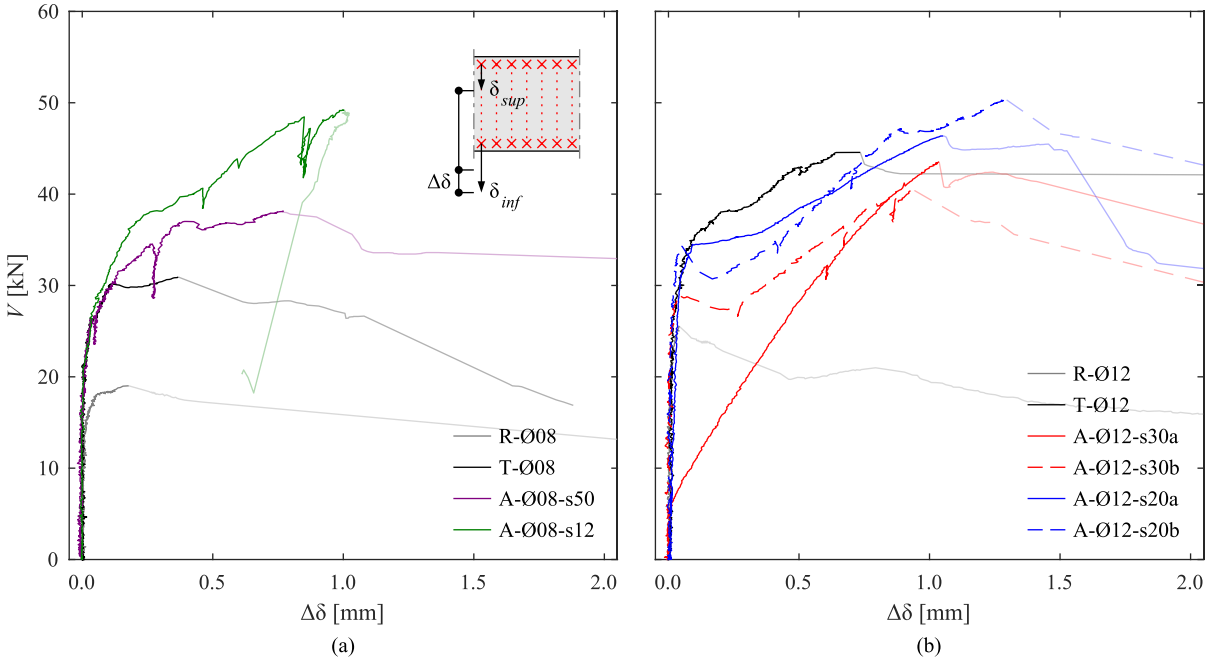

Fig. 12. Shear force (V) vs vertical component of the shear crack opening ($\Delta\delta$) determined from global deformations for specimens with reinforcing bar diameters of (a) Ø8 mm and (b) Ø12 mm, respectively.

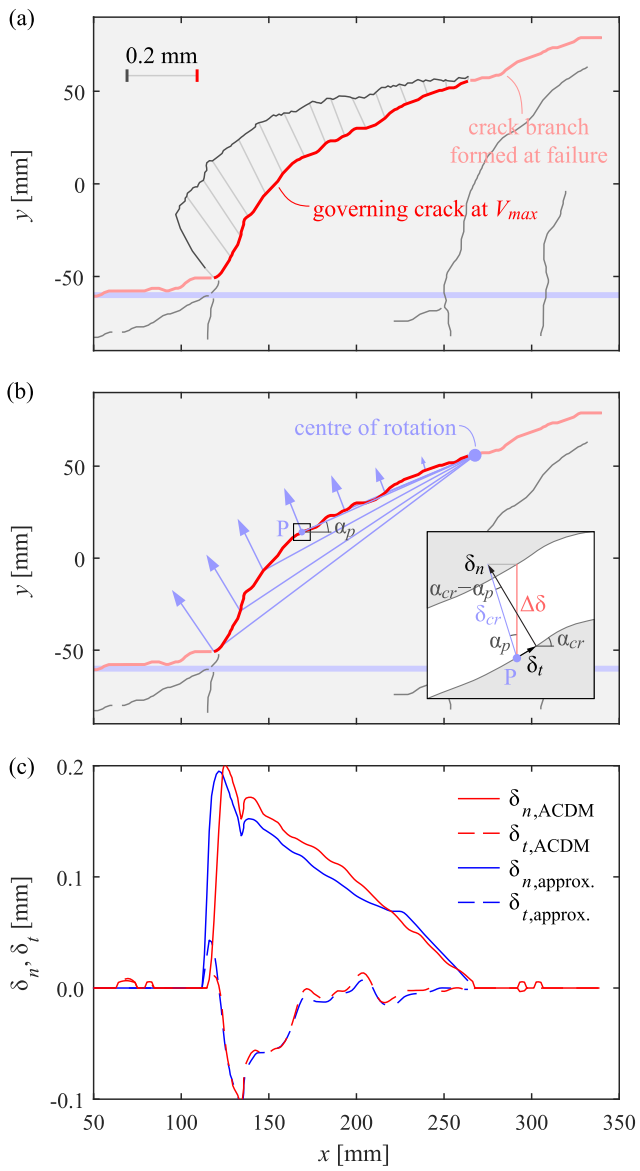

Fig. 13. Estimation of crack opening and slip from global deformations and validation with the reference specimen 'R-Ø12': (a) direct measurements of crack kinematics using ACDM, (b) determination of opening and slip from the vertical component of global deformations of the beam, (c) comparison of direct measurements and approximations.

direction, as illustrated in Fig. 13b, i.e.,

$$\delta_n = \Delta\delta \cdot \frac{\cos(\alpha_{cr} - \alpha_p)}{\cos(\alpha_p)} \tag{2}$$

$$\delta_t = \Delta\delta \cdot \frac{\sin(\alpha_{cr} - \alpha_p)}{\cos(\alpha_p)} \tag{3}$$

where $\Delta\delta$ = total vertical displacement in one section, α_{cr} = inclination of the crack, α_p = inclination of the line from the measuring point to the crack tip, as illustrated in Fig. 13b. The approach is validated with the reference specimen without textile ('R-Ø12'), where the direct measurements of the crack kinematics were available from DIC and ACDM. Fig. 13c compares the direct measurements of the crack opening and slip (red curve) with the estimations using the proposed approach (blue curve), generally showing a good correspondence. The application to concrete beams with textiles is, however, linked to more uncertainties since one of the governing parameters for the estimation is the location of the crack tip. As already described, the propagation of the crack at higher load levels cannot be directly measured due to the smeared deformations. Furthermore, multiple cracks crossing the same section cannot be distinguished, leading to an overestimation of the crack opening. Here, the centre of rotation was assumed according to the idealised shape of the governing crack proposed by *Cavagnis et al.* [38], and the vertical crack opening was linearly interpolated in the regions where multiple shear cracks occurred. The estimations of the crack opening and slip using this approach are thus suitable of roughly indicating the range of deformations to validate the plausibility of the shear transfer mechanisms, but do not exhibit the same accuracy as direct measurements of the crack kinematics.

5. Estimation of the contributions to the shear transfer across the governing crack

Existing studies on the shear transfer across a governing crack in RC beams with and without transverse reinforcement based on refined measurements (e.g. [39,40]) showed that, besides the activation of the transverse reinforcement, the shear transfer mainly depends on the kinematics and the shape of the governing crack. While the stresses in the textile can be obtained from the deformations of the textile based on the DIC and DFOS measurements, the estimation of the crack kinematics as described in Section 4.4 is used here as an indicator for the crack kinematics and the resulting contribution from the concrete to the shear capacity of the governing crack, which are summarised in Table 4 and discussed in the following sections.

5.1. Textile reinforcement

The contribution of the textile reinforcement to the shear transfer was determined by adding the contribution of every inlay crossing the governing crack, estimated from the DIC and DFOS strain measurements. The shape of the governing crack was assessed from the inspection of the concrete surface on the front side after stripping the textile (solid green lines in Fig. 11). The representative strain in an individual aramid inlay ($\varepsilon_{t,i}$) was obtained as the 95%-quantile of the strains along the inlay to filter out the strain peaks in the DIC measurements at the edges of the area of interest and in the vicinity of cracks in the base textile between two adjacent high-strength rovings. The resulting shear strength provided by the textile reinforcement (V_{tw}) was then determined from.

$$V_{tw} = \sum_{i}^{n_{rov}} \varepsilon_{t,i} \cdot E_t \cdot A_{rov} \tag{4}$$

where A_{rov} = cross-sectional area of one roving, n_{rov} = number of rovings crossing the governing crack. Where no measurements from DFOS were available, the corresponding measurement from DIC on the front side was used instead. The contribution of the epoxy-coated base textile was neglected due to its considerably lower stiffness and strength, as observed in the previous studies on weft-knitted textile reinforcement presented in [17–19]. The textile forces based on the measured strains (V_{tw}) are compared to the theoretical maximum shear strength ($V_{tw,nom}$) when considering the full tensile strength (f_t) of all inlays crossing the governing crack in Table 4, indicating low utilisation of the textile reinforcement (between 38% and 65%) owing to the lack of ductility in the material behaviour of the aramid rovings, leading to a progressive failure once the first inlay reached its tensile strength. Fig. 14 shows the maximum strains in the textile ($\varepsilon_{tw,max}$) over the specimen height plotted against the length of the governing shear span of Specimens 'A-Ø12-s30a' and 'A-Ø12-s30b' at ultimate load. The dotted lines indicate the position of the inlays on the front of the specimen, where the deformations were assessed with DIC. The measurements from the fibre optical sensing are denoted as '+'. While the strains in Specimen 'A-Ø12-s30b' were generally well below the failure strain, there were some

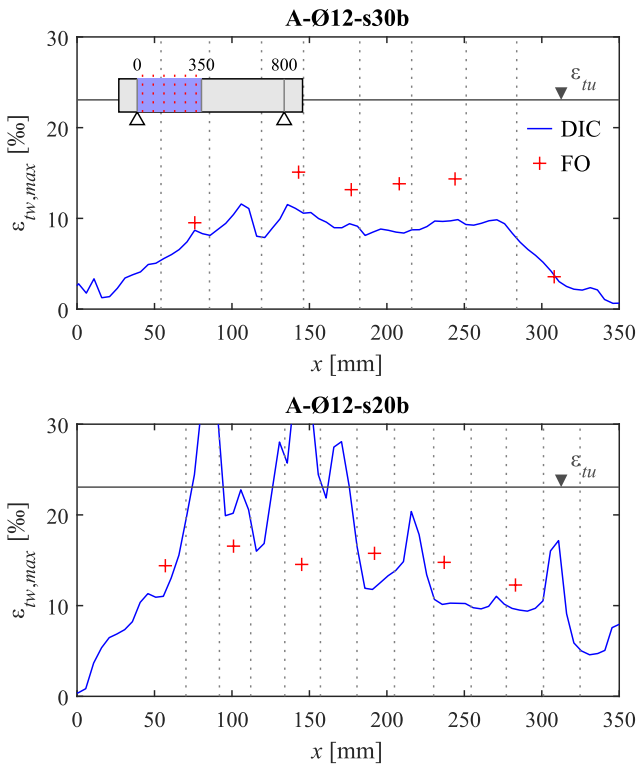

Fig. 14. Measurements of the maximum textile strains along the governing span at ultimate load based on DIC on the front side (blue line) and DFOS on the back side (red crosses) for Specimens' A-Ø12s30b' and 'A-Ø12s20b' (dotted grey lines = location of the aramid inlays crossing the governing crack on the front side of the specimen).

distinct local peaks in Specimen 'A-Ø12-s20b'. These local peaks occurred mostly between two adjacent inlays within the epoxy-coated base textile. The slight exceedance of the failure strain for some inlays lies still within the scatter of the material properties. Furthermore, the high strain area caused by the cracks within the base textile might have been smeared over a larger area, distorting the very local measurement of the strain in the inlay. The differences in the measurements based on DIC and DFOS depend on the different degrees of debonding of the textile between the front and the back side, which lead to a more or less pronounced concentration of the strains over the length of the inlay (=specimen height).

5.2. Concrete contribution

The contribution of the concrete to the shear capacity mainly consists of the following phenomena [41,42]: (i) aggregate interlock, (ii) shear in compression zone (=direct strut), and (iii) residual tensile stresses in the fracture process zone. The latter is essentially dependent on the crack kinematics at the crack tip, whose estimation is subject to high uncertainty in this study, as described in Section 4.4, and is, therefore, omitted. While the residual tensile stresses can have a significant influence on the shear capacity of concrete beams without transverse reinforcement [40], studies on shear beams with transverse reinforcement [39] showed that their influence was negligible compared to the other shear transfer mechanisms.

5.2.1. Aggregate interlock

The ability of concrete to transfer stresses across cracks is primarily due to aggregate interlock. The rough surface of the crack face leads to the development of normal and tangential stresses, which are dependent on the crack opening and slip. Several models have been proposed in the literature to estimate the aggregate interlock stresses [43–45], whereby the calculated stresses for given crack kinematics often exhibit relatively large differences depending on the applied model [46]. The present study relies on the Two-Phase-Model proposed by *Walraven* [43] due to its physically-based definition of the contact area between the aggregates and the cement matrix. Hence, the normal (σ_{ag}) and shear (τ_{ag}) stresses at the interface are determined from.

$$\sigma_{ag} = \sigma_{pu} \cdot (A_t - \mu \cdot A_n) \tag{5}$$

$$\tau_{ag} = \sigma_{pu} \cdot (A_n + \mu \cdot A_t) \tag{6}$$

where $\sigma_{pu} = 6.39 \cdot f_{c,cube}^{0.56}$ with $f_{c,cyl} = 0.8 \cdot f_{c,cube}$, $\mu = 0.4$ = friction coefficient between the aggregate and the matrix, A_n, A_t = average contact areas between aggregates and cement matrix perpendicular and parallel to the crack edge, respectively, which have to be determined numerically and are dependent on the crack opening and slip, and the maximum aggregate size D_{max}. The crack kinematics at ultimate load were estimated according to the approach described in Section 4.4. The shear strength from aggregate interlock (V_{ag}) then follows from

$$V_{ag} = b \cdot \left(\int_0^{l_{cr}} \tau_{ag} \cdot \sin(\alpha_{cr}(t)) \cdot dt + \int_0^{l_{cr}} \sigma_{ag} \cdot \cos(\alpha_{cr}(t)) \cdot dt \right) \tag{7}$$

where b = width of the specimen, l_{cr} = length of the crack, α_{cr} = inclination of the crack. The resulting contributions from aggregate interlock are summarised in Table 4.

The shear strength provided by aggregate interlock was in a reasonable range for the reference specimens ('R-Ø08' and 'R-Ø12'), where the direct measurements of the crack openings and slips from ACDM were available. All specimens with textiles (both with and without high-strength inlays) displayed rather low contributions from aggregate interlock due to the larger crack openings at failure.

5.2.2. Direct strut

The low shear slenderness in the short span of the beam basically allowed the formation of a direct strut from the load application to the support. The capacity of the concrete to transfer the related stresses is highly dependent on the crack pattern and kinematics. *Cavagnis et al.* [40] showed that the contribution of the direct strut may be dominant for the shear transfer if the governing crack did not penetrate into the strut. The compressive strains measured in the textile differed from the concrete strains due to debonding, and cannot be directly used for the calculation of concrete stresses, and eventually, the quantitative estimation of the contribution from the direct strut. However, the direction and the magnitudes of the principal strains allow a qualitative assessment of the load-bearing behaviour. Fig. 15 shows exemplary results of principal compressive strains at ultimate load for specimens (a) without textile ('R-Ø12'), (b) with epoxy-coated textile but without inlays ('T-Ø12'), and (c) with aramid inlays at a spacing of 30 mm ('A-Ø12-s30b'). The governing cracks in the concrete are shown as solid green lines. Note that the governing cracks in the concrete were assessed after the failure for the specimens with textiles, and the crack presumably had not propagated as far into the depth of the compression zone at the peak load. The compressive strains in the reference specimen without textile were not very high but seemed to align fairly horizontally at the compression chord (Fig. 15a). The crack was located rather near the support, which hindered the formation of a direct strut due to the crack crossing its theoretical line of action. Both specimens with textiles (with and without high-strength inlays) exhibited pronounced inclinations of the principal strains, but the different crack geometries suggest a fundamentally different load-bearing behaviour. In the specimen without high-strength inlays (Fig. 15b), the compressive strains followed the direction of the governing crack, which had a steep inclination and formed close to the load introduction, allowing the compressive stresses to be transferred within the uncracked concrete. The strut did not directly lead to the support but followed the branching crack, which

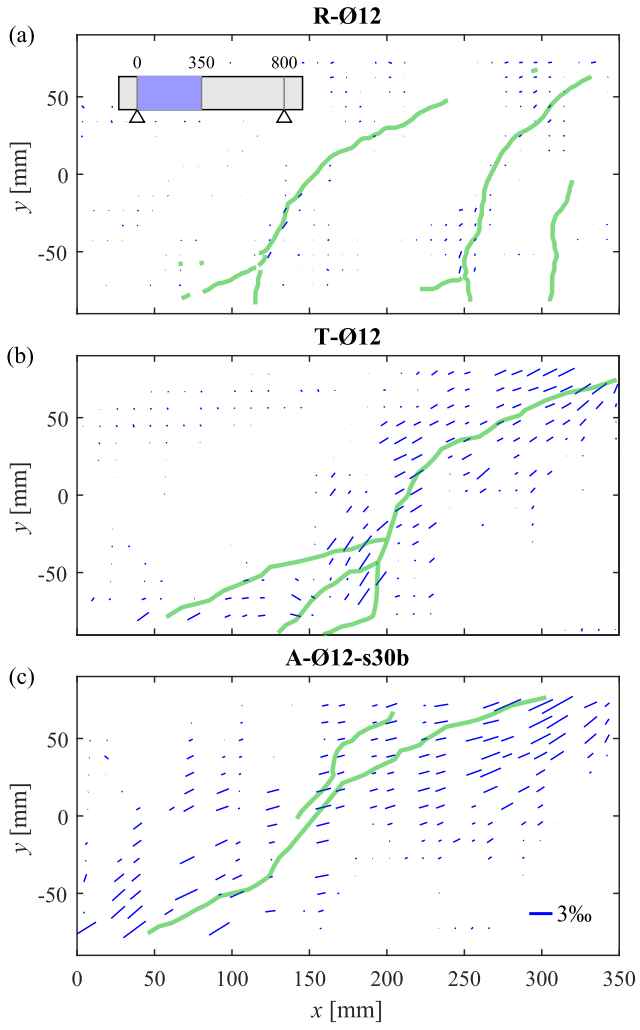

Fig. 15. Direction and normalised magnitudes of compressive strains in governing span for Specimens (a) 'R-Ø12', (b) 'T-Ø12', and (c) 'A-Ø12-s30b' (with crack pattern denoted as green lines).

probably formed due to the contribution from dowel action, see Section 5.3. The governing crack in the specimen with aramid inlays had a flatter inclination (Fig. 15c), with most of the compressive strains crossing the crack nearly horizontally since the vertically aligned textile reinforcement was activated in tension, bridging the opening crack. In the specimens 'R-Ø08', 'A-Ø12-30a', and 'A-Ø12-20a', the governing crack did not cross the compression strut due to its close location to the load introduction or its flat inclination; thus, the action of a direct strut presumably led to the formation of the failure crack in the long span. While the influence of the direct strut seems to be significant in the load-bearing behaviour of the examined beams with relatively low shear slenderness, it is expected that its contribution may decrease for higher shear slendernesses ($a/d > 3$) since it is more likely for the compression strut to intersect the governing crack due to its lower inclination, as described in [39].

5.3. Dowel action

Besides their primary purpose to guarantee the flexural capacity of the concrete beams, the longitudinal steel reinforcing bars contribute to the shear transfer across the governing crack by transferring forces perpendicular to their axes [47]. Its magnitude essentially depends on the vertical displacements of the bars. While there are several experimental investigations in the literature examining this phenomenon (e.g. [48]), the present study applies the analytical approach proposed by *Cavagnis et al.* [40], which estimates the contribution to the shear strength from the flexural deformation of the reinforcing bar, assuming a linear elastic behaviour. The deflections are approximated using a third-order polynomial based on the surface measurements from DIC in the vicinity of the governing shear crack and the branching dowel crack, as illustrated in Fig. 16. Differentiating the deflections three times and assuming that the GFRP rods in the tension chord adopted the same deflection curve as the steel reinforcing bars yields the shear force carried by dowel action (V_{dow}):

$$V_{dow} = \left(n_s \cdot E_s \cdot I_s + n_{gf} \cdot E_{gf} \cdot I_{gf}\right) \cdot \frac{d^3\delta(x)}{dx^3} = \frac{12 \cdot \left(n_s \cdot E_s \cdot I_s + n_{gf} \cdot E_{gf} \cdot I_{gf}\right)}{l_{dow}^3} \cdot \left(\delta_1 - \delta_0 + \frac{l_{dow}}{2} \cdot \left(\delta_0' + \delta_1'\right)\right) \quad (8)$$

where n_s = number, E_s = Young's modulus, and I_s = moment of inertia of the steel reinforcing bars, respectively; n_{gf} = number, E_{gf} = Young's modulus, and I_{gf} = moment of inertia of the GFRP rods, respectively; δ_0, δ_1 = deflections, and δ_0', δ_1' = slopes of the reinforcing bar at the dowel crack, respectively.

The deflections and slopes were determined at a distance of half a bar diameter from the intersection of the governing shear crack and the dowel crack with the longitudinal reinforcing bar, respectively, as illustrated in Fig. 16. The resulting shear forces from dowel action are summarised in Table 4. While most of the beams displayed moderate contributions from dowel action, Specimen 'T-Ø12' exhibited a substantial shear force, which might have supported the direct strut, as described in Section 5.2.2.

5.4. Discussion on the validity of the models

The comparison of the experimentally observed shear capacities (V_{exp}) and the sum of various contributions to the shear transfer across the governing crack based on the deformation measurements ($\sum V_i = V_{tw} + V_{ag} + V_{dow}$) exhibits large deviations (see rightmost columns of Table 4). While existing literature highlights the possibilities arising from refined measurements [39,40], most estimation procedures rely on the detailed assessment of the crack pattern and kinematics, which could partly only be indirectly obtained in this study, making use of several assumptions. The estimations of the aggregate interlock forces were close to zero for all specimens with textiles (with and without high-strength inlays). Here, the estimation of the crack opening and slip is essentially dependent on the location of the crack tip, which was determined on manually assessed crack geometries after failure. In the reference specimens, where direct measurements of the crack

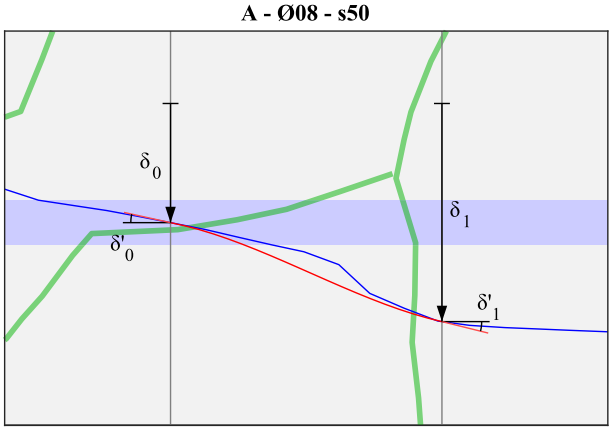

Fig. 16. Deformations of the flexural reinforcement in the vicinity of the dowel crack of Specimen 'A-Ø08-s50': measurements based on DIC (blue line) and third-order polynomial approximation (red line).

kinematics were available, the combination of the estimated contributions to the shear transfer across the governing crack agreed better with the measured shear capacity. This result emphasises the importance of precise measurements and the reliable assessment of the crack geometry and kinematics. The activation of the aramid inlays could be directly obtained from the surface deformations of the textile and yielded reasonable results regarding the increase of shear strength for higher transverse reinforcement ratios, and indicated that the brittle material behaviour prevents the full exploitation of the tensile capacity. The dowel action was estimated based on simple but mechanically sound assumptions, which, however, rely on the surface displacements of the beam and the crack patterns obtained from visual inspection, whose accuracy lies in the range of a few millimetres. The actual deformation of the reinforcing bars, which was presumably slightly different, could have been assessed more accurately using DFOS measurements along the reinforcing bar, as suggested in [49]. The estimations are still useful for explaining peculiar results, such as the surprisingly high shear strength of Specimen 'T-Ø12′ without high-strength inlays, which could be partially attributed to the dowel action, as discussed in Section 5.3 and Table 4. The direct strut, which cannot be quantified in the specimens with tubular textiles due to the impossibility to measure the concrete deformations, appears to be the major shear contribution in these specimens since the combined contributions of all quantified mechanisms merely explains 30–60% of the resistance.

While the lack of direct measurements of the crack kinematics generally hindered the reliable quantitative assessment of the shear transfer contributions from the concrete, the meticulous analysis of the deformations of the specimens revealed fundamental insights for understanding the load-bearing behaviour, such as the contribution from a direct strut, which is highly dependent on the crack pattern and could be qualitatively studied using the principal compressive strains obtained from DIC.

6. Conclusions

The present study investigated the potential of stay-in-place formworks with integrated textile reinforcement to increase the shear capacity of concrete beams with conventional longitudinal steel reinforcing bars. Tubular weft-knitted textiles present many possibilities for various cross-section geometries when using shaping elements, such as cables or bending-active rods. The feasibility of the manufacturing procedure and the structural performance were validated in an experimental campaign consisting of ten specimens with rectangular cross-sections. The reinforcing approach ensured the proper anchorage of the shear reinforcement by means of continuous winding around the cross-section, in contrast to conventional textile reinforcement, which usually requires lap splices and a certain anchorage length.

Compared to the reference specimens without any shear reinforcement, the beams with textiles exhibited a considerably higher shear capacity even without the integration of high-strength inlays, whereby the failure mode remained brittle. The increase in the transverse reinforcement ratio led to a fairly linear increase in the failure load. The only exception was one specimen without high-strength inlays, which exhibited a surprisingly high peak load (+50% compared to the corresponding specimen with the same textile configuration but with a lower longitudinal reinforcement ratio), even exceeding those of the specimens with aramid inlays. The consideration of various contributions to the shear transfer across the governing crack revealed that the shear capacity is highly dependent on the crack pattern. However, the contributions from the concrete to the load-bearing behaviour were difficult to assess since the concrete compressive strains and crack kinematics could not be directly measured due to the presence of the textile on the outer surface of the concrete beam. Therefore, the crack opening and slip were determined based on the global deformations of the beam and the crack patterns from visual inspection after testing. While the estimations of the aggregate interlock forces led to reasonable results for the reference specimens (accounting for 50% to 100% of the resisted shear force), where the direct measurements of the crack kinematics were available, the specimens with textiles (with and without high-strength inlays) exhibited contributions close to zero. While it is clear that larger crack openings lead to smaller aggregate interlock stresses, the results need to be treated with caution due to the dependence of the procedure on exact crack measurements. The qualitative consideration of the compressive strains over the surface of the beams showed the substantial influence of the direct transfer of the compression forces from the load introduction to the support, which strongly depends on the shape of the governing crack. The dowel action of the longitudinal reinforcing bars and the GFRP rods had a minor role for most beams, except the specimen without high-strength inlays, where significant dowel action could explain the surprisingly high shear strength.

The strains in the textile could be directly obtained from the DIC and DFOS measurements. The low bond shear stresses between textile and concrete led to the delamination of the textile with increasing deformations, causing a spread of strains over a larger area rather than being concentrated in the vicinity of the crack. However, it was not possible to reach the full tensile capacity of the shear reinforcement (utilisations between 40% and 65%) due to the brittle behaviour of the aramid inlays and the consequent progressive failure once the first roving reached its tensile strength. The beam with the highest amount of aramid inlays resisted the shear loading until, eventually, a bending failure due to the rupture of the longitudinal steel reinforcing bars at large deformations occurred. The combination of a brittle material, i.e. epoxy-coated continuous aramid fibres, as shear reinforcement with a ductile material, i.e. deformed steel bars, as flexural reinforcement proved to be successful in achieving large deformation capacity in this specimen.

The manufacturing procedure and the validation of the structural performance in the experimental campaign showed the potential of weft-knitted flexible formworks with integrated high-strength inlays, which enable a wide spectrum of cross-section types and opportunities for material-efficient concrete structures. However, the vertical casting position limits the range of feasible spans, which should be addressed in further developments of the flexible formwork systems, allowing the concrete to be filled from the top face of the cross-section as in conventional concrete construction. While the rectangular cross-sections presented in this study allowed a detailed consideration of the deformations, which significantly helped to understand the load-bearing behaviour, the resulting relatively low transverse reinforcement ratio led to a rather dominant contribution from the concrete to the shear transfer capacity across the governing crack when compared to the aramid inlays. To improve the understanding of the load-bearing behaviour dependent on the deformations of the reinforcement and the concrete, comparative investigations using finite element analyses may be the subject of future research. Furthermore, thin-walled cross-sections using textile reinforcement may lead to further optimisation of the material consumption and would likely enable a more reliable assessment of the shear strength.

CRediT authorship contribution statement

Minu Lee: Conceptualization, Methodology, Investigation, Visualization, Writing – original draft. **Jaime Mata-Falcón:** Conceptualization, Methodology, Writing – review & editing, Supervision. **Walter Kaufmann:** Conceptualization, Funding acquisition, Writing – review & editing.

Declaration of Competing Interest

The authors declare that they have no known competing financial interests or personal relationships that could have appeared to influence the work reported in this paper.

Data availability

The experimental data presented in this article was submitted to a public data repository and is published under the following https://doi.org/10.3929/ethz-b-000546394.

Acknowledgements

The authors gratefully acknowledge Prof. Dr Mariana Popescu from TU Delft (manufacturing of the knitted textiles) and Tena Galkovski from the Institute of Structural Engineering at ETH Zürich (instrumentation of the specimens using distributed fibre optical sensing) for contributing their technical and practical expertise and the Master's students Fiorentina Ademi, Tim Cousin and Stefan Liniger for their valuable support during the preparation of the specimens. This research is supported by the National Centre for Competence in Research in Digital Fabrication, funded by the Swiss National Science Foundation (project number 51NF40-141853).

Open access data

The experimental data presented in this article was submitted to a public data repository and is published under the following DOI: 10.3929/ethz-b-000546394

References

[1] Curbach M, editor. Sachstandbericht zum Einsatz von Textilien im Massivbau. Berlin: Beuth; 1998.
[2] Hegger J, Horstmann M, Voss S, Will N. Textilbewehrter Beton: Tragverhalten, Bemessung und Anwendung. Beton- Stahlbetonbau 2007;102:362–70. https://doi.org/10.1002/best.200700552.
[3] Fernàndez Ruiz M, Muttoni A. Building in a lighter and more sustainable manner: textile reinforced concrete for thin structural elements. cemsuisse 2017.
[4] Hegger J, Kulas C, Schneider HN, Brameshuber W, Hinzen M, Raupach M, et al. TRC pedestrian bridge - design, load-bearing behavior and production processes of a slender and lightweight construction. In: Brameshuber W, editor., Aachen: RILEM Publications SARL; 2010.
[5] Hegger J, Curbach M, Stark A, Wilhelm S, Farwig K. Innovative design concepts: application of textile reinforced concrete to shell structures. Struct Concr 2018;19:637–46. https://doi.org/10.1002/suco.201700157.
[6] Valeri P, Guaita P, Baur R, Fernández Ruiz M, Fernández-Ordóñez D, Muttoni A. Textile reinforced concrete for sustainable structures: future perspectives and application to a prototype pavilion. Struct Concr 2020;21:2251–67. https://doi.org/10.1002/suco.201900511.
[7] Peled A, Mobasher B, Bentur A. Textile reinforced concrete. Boca Raton, FL: CRC Press, Taylor & Francis Group; 2017.
[8] Preinstorfer P, Kromoser B, Kollegger J. Flexural behaviour of filigree slab elements made of carbon reinforced UHPC. Constr Build Mater 2019;199:416–23. https://doi.org/10.1016/j.conbuildmat.2018.12.027.
[9] Kromoser B, Preinstorfer P, Kollegger J. Building lightweight structures with carbon-fiber-reinforced polymer-reinforced ultra-high-performance concrete: research approach, construction materials, and conceptual design of three building components. Struct Concr 2019;20:730–44. https://doi.org/10.1002/suco.201700225.
[10] Valeri P, Ruiz MF, Muttoni A. Modelling of textile reinforced concrete in bending and shear with elastic-cracked stress fields. Eng Struct 2020;215:110664. https://doi.org/10.1016/j.engstruct.2020.110664.
[11] Yang Y, Orr J, Spadea S. Shear behavior of variable-depth concrete beams with wound fiber-reinforced polymer shear reinforcement. J Compos Constr 2018;22:04018058. https://doi.org/10.1061/(ASCE)CC.1943-5614.0000899.
[12] Veenendaal D, West M, Block P. History and overview of fabric formwork: using fabrics for concrete casting. Struct Concr 2011;12:164–77. https://doi.org/10.1002/suco.201100014.
[13] Hawkins WJ, Herrmann M, Ibell TJ, Kromoser B, Michaelski A, Orr JJ, et al. Flexible formwork technologies - a state of the art review. Struct Concr 2016;17(6):911–35.
[14] Orr JJ, Darby A, Ibell TJ, Evernden M, Otlet M. Concrete structures using fabric formwork 2017. https://doi.org/10.17863/cam.17019.
[15] Popescu M, Reiter L, Liew A, Van Mele T, Flatt RJ, Block P. Building in concrete with an ultra-lightweight knitted stay-in-place formwork: prototype of a concrete shell bridge. Structures 2018;14:322–32. https://doi.org/10.1016/j.istruc.2018.03.001.
[16] Popescu M, Rippmann M, Liew A, Reiter L, Flatt RJ, Van Mele T, et al. Structural design, digital fabrication and construction of the cable-net and knitted formwork of the KnitCandela concrete shell. Structures 2021;31:1287–99.
[17] Lee M, Mata-Falcón J, Kaufmann W. Load-deformation behaviour of weft-knitted textile reinforced concrete in uniaxial tension. Mater Struct 2021;54:210. https://doi.org/10.1617/s11527-021-01797-5.
[18] Lee M, Mata-Falcón J, Kaufmann W. Analysis of the tension chord in the flexural response of concrete elements: methodology and application to weft-knitted textile reinforcement. Eng Struct 2022;261:114270.
[19] Lee M, Mata-Falcón J, Kaufmann W. Influence of short glass fibres and spatial features on the mechanical behaviour of weft-knitted textile reinforced concrete elements in bending. Constr Build Mater 2022;344:128167. https://doi.org/10.1016/j.conbuildmat.2022.128167.
[20] Popescu M, Rippmann M, Van Mele T, Block P. Complex concrete casting: knitting stay-in-place formwork. Proceedings of the IASS 2016 Tokyo Symposium: Spatial Structures in the 21st Century, Tokyo, Japan: The International Association for Shell and Spatial Structures (IASS), Laboratorio Central de Estructuras y Materiales (CEDEX); 2016, p. 1278.
[21] Popescu M. KnitCrete: Stay-in-place knitted formworks for complex concrete structures. ETH Zurich 2019. https://doi.org/10.3929/ETHZ-B-000408640.
[22] Lee M, Mata-Falcón J, Popescu M, Block P, Kaufmann W. Potential Approaches for Reinforcing Complex Concrete Structures with Integrated Flexible Formwork. In: Bos FP, Lucas SS, Wolfs RJM, Salet TAM, editors. Second RILEM International Conference on Concrete and Digital Fabrication, vol. 28, Cham: Springer International Publishing; 2020, p. 669–79. https://doi.org/10.1007/978-3-030-49916-7_67.
[23] Martens R. Zum Tragverhalten von Betonplatten mit integrierten Schalungselementen. Doctoral dissertation. Institut für Baustatik und Konstruktion. ETH Zürich 1997. https://doi.org/10.3929/ethz-a-001853800.
[24] Steinle A, Bachmann H, Tillmann M. Bauen mit Betonfertigteilen im Hochbau. In: Bergmeister K, Fingerloos F, Wörner J-D, editors. Beton-Kalender 2016, Berlin, Germany: Wilhelm Ernst & Sohn, Verlag für Architektur und technische Wissenschaften GmbH & Co. KG; 2016, p. 237–467. https://doi.org/10.1002/9783433603413.ch3.
[25] Kurz W, Mensinger M, Sauerborn I, Sauerborn N, Claßen M. Verbundträger und Deckensysteme. In: Kuhlmann U, editor. Stahlbau Kalender 2018. 1st ed., Wiley; 2018, p. 435–522. https://doi.org/10.1002/9783433607701.ch4.
[26] Boccadoro L, Frangi A. Experimental analysis of the structural behavior of timber-concrete composite slabs made of beech-laminated veneer lumber. J Perform Constr Facil 2014;28:A4014006. https://doi.org/10.1061/(ASCE)CF.1943-5509.0000552.
[27] Verbruggen S, Remy O, Wastiels J, Tysmans T. Stay-in-place formwork of TRC designed as shear reinforcement for concrete beams. Adv Mater Sci Eng 2013;2013:1–9.
[28] De Sutter S, Remy O, Tysmans T, Wastiels J. Development and experimental validation of a lightweight stay-in-place composite formwork for concrete beams. Constr Build Mater 2014;63:33–9. https://doi.org/10.1016/j.conbuildmat.2014.03.032.
[29] Burger J, Lloret-Fritschi E, Scotto F, Demoulin T, Gebhard L, Mata-Falcón J, et al. Eggshell: ultra-thin three-dimensional printed formwork for concrete structures. 3D Printing Additive Manufact 2020;7(2):48–59.
[30] Lloret-Fritschi E, Wangler T, Gebhard L, Mata-Falcón J, Mantellato S, Scotto F, et al. From smart dynamic casting to a growing family of digital casting systems. Cem Concr Res 2020;134:106071.
[31] R&G Faserverbundwerkstoffe GmbH. Technische Daten -. Epoxydharz L 2020.
[32] Marti P. Size Effect in Double-Punch Tests on Concrete Cylinders. MJ 1989;86:597–601. https://doi.org/10.14359/2261.
[33] Correlated Solutions. Vic-3D Software Manual. Correlated Solutions Inc.; 2019.
[34] Fachbereich Prozessmesstechnik und Strukturanalyse. VDI/VDE 2626 Blatt 1 - Optische Messverfahren - Bildkorrelationsverfahren - Grundlagen und Begriffe. VDI/VDE-Gesellschaft Mess- und Automatisierungstechnik; 2018.
[35] Mata-Falcón J, Haefliger S, Lee M, Galkovski T, Gehri N. Combined application of distributed fibre optical and digital image correlation measurements to structural concrete experiments. Eng Struct 2020;225:111309. https://doi.org/10.1016/j.engstruct.2020.111309.
[36] Gehri N, Mata-Falcón J, Kaufmann W. Automated crack detection and measurement based on digital image correlation. Constr Build Mater 2020;256:119383. https://doi.org/10.1016/j.conbuildmat.2020.119383.
[37] Gehri N, Mata-Falcón J, Kaufmann W. Refined extraction of crack characteristics in Large-scale concrete experiments based on digital image correlation. Eng Struct 2022;251:113486. https://doi.org/10.1016/j.engstruct.2021.113486.
[38] Cavagnis F, Simões JT, Ruiz MF, Muttoni A. Shear strength of members without transverse reinforcement based on development of critical shear crack. SJ 2020;117:103–18. https://doi.org/10.14359/51718012.
[39] Huber P, Huber T, Kollegger J. Investigation of the shear behavior of RC beams on the basis of measured crack kinematics. Eng Struct 2016;113:41–58. https://doi.org/10.1016/j.engstruct.2016.01.025.
[40] Cavagnis F, Ruiz MF, Muttoni A. An analysis of the shear-transfer actions in reinforced concrete members without transverse reinforcement based on refined experimental measurements. Struct Concr 2017:1–16. https://doi.org/10.1002/suco.201700145.
[41] fib Bulletin 57. Shear and punching shear in RC and FRC elements. Lausanne: 2010.
[42] ASCE-ACI Committee 445 on Shear and Torsion. Recent approaches to shear design of structural concrete. J Struct Eng 1998;124:1375–417. https://doi.org/10.1061/(ASCE)0733-9445(1998)124:12(1375).
[43] Walraven JC. Fundamental analysis of aggregate interlock. J Struct Div ASCE 1981;107(11):2245–70.
[44] Gambarova P, Karakoç C. A new approach to the analysis of the confinement role in regularly cracked concrete elements. In: International Association for Structural

Mechanics in Reactor Technology, editor. Transactions of the 7th International Conference on Structural Mechanics in Reactor Technology, Chicago, Illinois, U.S. A., August 22 - 26, 1983. Vol. M: Reliability and risk analysis of nuclear power plants, Amsterdam: North-Holland Physics Publ; 1983, p. 251–61.

[45] Li B, Maekawa K. Contact density model for cracks in concrete. IABSE Reports 1987;54:51–62.

[46] Beck A. Paradigms of shear in structural concrete: Theoretical and experimental investigation. Doctoral Thesis. ETH Zurich, 2021. https://doi.org/10.3929/ethz-b-000482684.

[47] Mörsch E. Der Eisenbetonbau - Seine Theorie und Anwendung (Reinforced Concrete Construction – Theory and Application). vol. 3. Auflage, 1908, 376 pp., 5. Auflage, 1. Band, 1. Hälfte, 1920, 471 pp., 2. Hälfte, 1922, 460 pp. Stuttgart: Verlag Konrad Wittwer; 1908.

[48] Baumann T, Rüsch H. Schubversuche mit indirekter Krafteinleitung: Versuche zum Studium der Verdübelungswirkung der Biegezugbewehrung eines Stahlbetonbalkens. vol. 210. Berlin: Ernst & Sohn; 1970.

[49] Galkovski T, Lemcherreq Y, Mata-Falcón J, Kaufmann W. Fundamental studies on the use of distributed fibre optical sensing on concrete and reinforcing bars. Sensors 2021;21:7643. https://doi.org/10.3390/s21227643.